

Article

Inductive Power Transfer Subsystem for Integrated Motor Drive

Zbigniew Kaczmarczyk¹, Marcin Kasprzak¹, Adam Ruszczyk², Kacper Sowa² , Piotr Zimoch^{1,*} ,
Krzysztof Przybyła¹ and Kamil Kierepka¹ 

¹ Department of Power Electronics, Electrical Drive and Robotics, Silesian University of Technology, 44100 Gliwice, Poland; Zbigniew.Kaczmarczyk@polsl.pl (Z.K.); Marcin.Kasprzak@polsl.pl (M.K.); Krzysztof.Przybyla@polsl.pl (K.P.); Kamil.Kierepka@polsl.pl (K.K.)

² ABB Corporate Technology Center, 31038 Cracow, Poland; adam.ruszczyk@pl.abb.com (A.R.); Kacper.Sowa@pl.abb.com (K.S.)

* Correspondence: Piotr.Zimoch@polsl.pl; Tel.: +48-32-237-12-47

Abstract: An inductive power transfer subsystem for an integrated motor drive is presented in this paper. First, the concept of an integrated motor drive system is overviewed, and its main components are described. Next, the paper is focused on its inductive power transfer subsystem, which includes a magnetically coupled resonant circuit and two-stage energy conversion with an appropriate control method. Simplified complex domain analysis of the magnetically coupled resonant circuit is provided and the applied procedure for its component selection is explained. Furthermore, the prototype of the integrated motor drive system with its control is described. Finally, the prototype based on the gallium nitride field effect transistors (GaN FET) inductive power transfer subsystem is experimentally tested, confirming the feasibility of the concept.

Keywords: motor drives; wireless power transfer (WPT); inductive power transfer (IPT); coupled circuits; resonant converters



Citation: Kaczmarczyk, Z.; Kasprzak, M.; Ruszczyk, A.; Sowa, K.; Zimoch, P.; Przybyła, K.; Kierepka, K. Inductive Power Transfer Subsystem for Integrated Motor Drive. *Energies* **2021**, *14*, 1412. <https://doi.org/10.3390/en14051412>

Academic Editor: Alon Kuperman

Received: 19 January 2021

Accepted: 1 March 2021

Published: 4 March 2021

Publisher's Note: MDPI stays neutral with regard to jurisdictional claims in published maps and institutional affiliations.



Copyright: © 2021 by the authors. Licensee MDPI, Basel, Switzerland. This article is an open access article distributed under the terms and conditions of the Creative Commons Attribution (CC BY) license (<https://creativecommons.org/licenses/by/4.0/>).

1. Introduction

Wireless power transfer (WPT) has been an object of increased interest of researchers in recent years. Contactless energy transmission eliminates cables and connectors, thus increasing reliability. The technology is also naturally safe by providing electrical insulation. Inductive power transfer (IPT), which usually employs two magnetically coupled coils (forming a loosely coupled transformer) and compensation capacitors, is one of multiple technologies used for WPT [1–3]. IPT systems allow to achieve relatively long transmission distances with relatively high efficiencies. Their efficiencies depend heavily on the coupling coefficient between primary and secondary coils and their quality factors [4,5]. They can also supply multiple receivers [6]. IPT technology is a very popular solution for a wide range of applications [7–9], e.g., contactless charging of electric vehicles [10,11] and mobile devices [5], powering biomedical implants [4], flexible induction heating [12], or fluorescent lighting [13]. Recent advances in this regard relate to the structures of IPT systems [14–16], compensation circuits [15,17] and coil designs [5,18,19].

So far, little attention has been paid to the possibility of using IPT technology for motor drive systems. For example, [20] proposes a wireless in-wheel motor drive for electric vehicles to solve the problems with power cables and signal wires exposed to harsh environments. This system applies an additional controller and power converter at the motor side. In turn, in [21] a wireless bidirectional servo motor drive is described and [22] presents a wireless switched reluctance motor drive. In both cases the principles of the so-called “energy encryption” [23] and selective wireless power transfer [24] are applied. The reluctance motor drive in [22] is switched by using receiver coils of different resonant frequencies, while the servo motor drive in [21] is based on the same method for bidirectional motion. In [21] and [22], neither a controller nor a power converter at the secondary-side of the IPT system is used. In contrast to these studies, the solution

presented in this paper provides a fully functional electric motor drive system, which is integrated with motor housing. Importantly, the system is powered via a contactless plug which makes it suitable for specific applications. It can easily be adapted to all types of electric motors [25]. The developed system is composed of an electric motor connected to a dedicated drive, powered wirelessly by transmitter and receiver modules—a substitute for a regular plug. Therefore, the system is fully hermetic and dedicated to harsh environments, e.g., the food and beverage (F&B) industry. The average lifetime of motors in the F&B industry is about one month [26]. The main failure reasons are bearings or windings of the motors. Motors that have been in operation for more than a month are often replaced by new ones as part of preventive maintenance [27,28]. The most popular motors are rated in the range of 1 to 2 kW and are used in pumps, conveyors, compressors, and others. The F&B industry (similarly to the chemical industry) has very high requirements for clean and reliable operation due to the continuous production process. Any unpredicted stops and delays may damage semi-products used in production and increase operating costs. The system modularity is a valuable advantage, allowing for simple installation and quick replacement of a damaged module (drive with motor). Due to the complexity of the whole system, this paper is mainly focused on presenting the general concept of the developed system and in more detail on its IPT subsystem. This IPT subsystem has a fully load-independent voltage gain. Similar solutions are analyzed in [29–31], but the design method of the IPT subsystem given in this paper is simplified and appropriately adapted. At the same time, additional feedback is applied to ensure the required fully load-independent voltage gain.

Section 2 provides an overview of the integrated motor drive system and its structure. The selection of magnetically coupled resonant circuit components is given in Section 3. Section 4 describes the prototype of the integrated motor drive system, presenting the applied IPT subsystem and its control in detail. The results of experimental tests of the prototype are shown in Section 5. Finally, the conclusions are drawn in Section 6.

2. Concept of IPT-IMD System

The proposed IPT-IMD system includes the IPT subsystem powering the integrated motor drive (IMD), which consists of a variable-frequency drive (VFD) with an electric motor (M). First, it should be clarified that the IPT and IMD subsystems can be considered individually. The IPT subsystem provides the required power to the IMD subsystem under a variable load, and its DC output voltage aligned with to the DC input voltage contains the information about the set angular velocity of the motor. On the other hand, the IMD subsystem based on this voltage is responsible for obtaining the desired angular velocity. A 3D visualization of the system is presented in Figure 1 and its schematic is depicted in Figure 2.

The applied magnetically coupled coils are designed to be identical and to fit within the plastic casings. They are single-layer and spiral, wound with litz-wire. Additionally, the coils are shielded with 3F3 ferrite and aluminum plates. The casings are built to have the same dimensions as the motor housing. The IPT-IMD system can be divided into the following sections: the input (IN) consisting of the DC supply U_I with capacitor bank C_I , the primary-side GaN FET inverter (INV), the magnetically coupled resonant circuit (MCR circuit), the secondary-side bridge rectifier (REC) and the output load (OUT/IMD) consisting of a DC link with capacitor bank C_O and the VFD with the electric motor (M). The equivalent components for the MCR circuit are also shown on the schematic. Namely, the AC sinusoidal source u_1 on the primary-side, and the AC load resistance R_{OAC} equivalent to the DC load resistance R_{ODC} on the secondary-side.

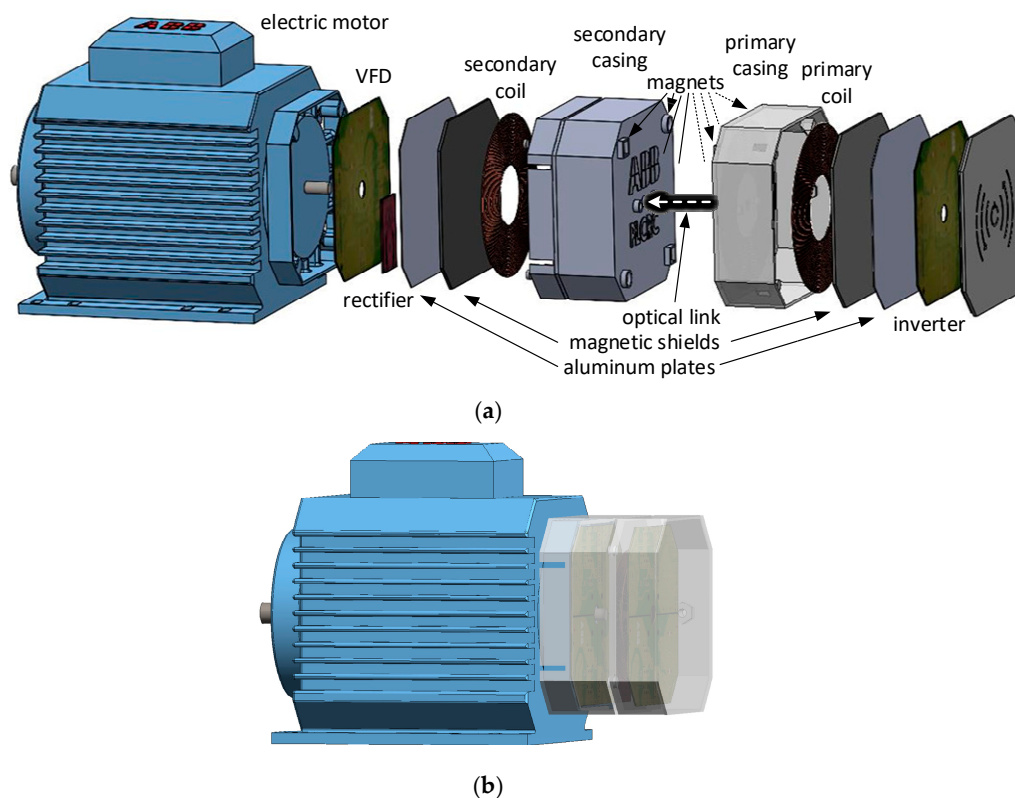


Figure 1. Visualization of IPT-IMD system: (a) disassembled, (b) assembled.

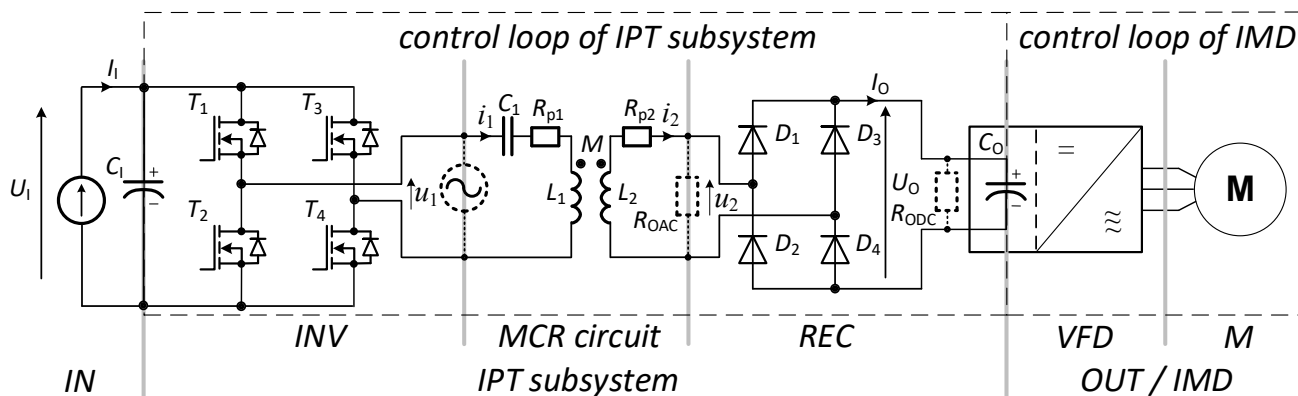


Figure 2. Schematic of the IPT-IMD system.

The angular velocity of the motor is controlled by the VFD, proportionally to the output voltage U_O , which varies with the input voltage U_I . In turn, the IPT subsystem is controlled to ensure the equality of U_I and U_O despite load variation. Therefore, the MCR circuit is designed accordingly, to make the output voltage stable in a wide range of load conditions and to be approximately 10% higher than the input voltage in case of open-loop operation. Additionally, an optical link is used as feedback information about the output voltage U_O for the IPT subsystem control in case of closed-loop operation. Further considerations are made under the assumption that the primary-side inverter switching frequency is 150 kHz and the input and output voltages should change in the range of 100 to 300 V, which relates to the full range of angular velocity of the considered motor (motor parameters are given in Section 4.3). The selected switching frequency ensures feasibility and acceptable power losses of the IPT-IMD system. It has a direct impact on the parameters of the magnetically coupled coils, which should be flat and properly fill the

plastic casings. Hence, their relatively high quality factors and strong magnetic coupling are obtained.

An additional component of the system is a set of magnets placed in the corners of both casings. In the event of a failure on either side of the system, it can be quickly plugged or unplugged without having to use any wires.

3. MCR Circuit Component Selection

A schematic of the MCR circuit is shown in Figure 3. It is assumed that passive components of the circuit are linear, invariant in time and ideal, except for the parasitic resistances of the coils. Overall, two series-series compensation capacitors are included in the circuit. The analysis is carried out using fundamental harmonic approximation in the complex domain—sinusoidal voltages and currents. The primary-side inverter is replaced by a voltage source \underline{U}_1 (1), while the rectifier is substituted by an equivalent resistance R_{OAC} (2)—Figure 2.

$$\frac{U_1}{U_1} = \frac{U_2}{U_O} = \frac{2\sqrt{2}}{\pi} \quad (1)$$

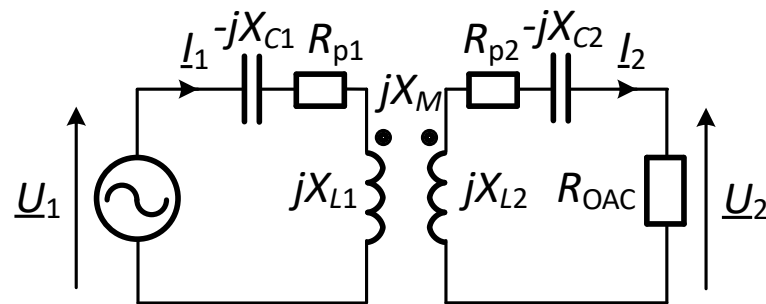


Figure 3. Schematic of MCR circuit.

U_1 and U_2 stand for root mean square (RMS) values of the input and output voltages.

$$\frac{R_{OAC}}{R_{ODC}} = \frac{8}{\pi^2} \quad (2)$$

The MCR circuit is described by the following equations:

$$\begin{aligned} \underline{U}_1 &= I_1(R_{p1} + j(X_{L1} - X_{C1})) - jkI_2\sqrt{X_{L1}X_{L2}} \\ \underline{U}_2 &= jkI_1\sqrt{X_{L1}X_{L2}} - I_2(R_{p2} + j(X_{L2} - X_{C2})), \\ \underline{U}_2 &= R_{OAC}I_2 \end{aligned} \quad (3)$$

where R_{p1} and R_{p2} are the parasitic resistances of the coils. The mutual reactance X_M is expressed by the coils' self-reactance values X_{L1} , X_{L2} and the coupling coefficient k .

Previous works [29–31] show that in the analyzed series-series compensated circuit it is possible to obtain the output voltage U_2 , which is nearly invariant with changes in the load resistance R_{OAC} and proportional to the input voltage U_1 . Complete invariance can only be obtained if the circuit is lossless ($R_{p1} = R_{p2} = 0$). If the coils' quality factors Q_1 and Q_2 (4) are high, the output voltage does not change much. Additionally, if the coils are strongly coupled ($k > 0.8$ —[32]) the efficiency is also high.

$$Q_1 = \frac{X_{L1}}{R_{p1}}, \quad Q_2 = \frac{X_{L2}}{R_{p2}} \quad (4)$$

Further analysis is done for the special case of the IPT subsystem—the output voltage U_O should be approximately 10% higher than the input voltage U_I in open-loop operation and the coils should be roughly similar. Initially, the analysis is simplified by assuming the

circuit to be lossless ($R_{p1} = R_{p2} = 0$). By applying Thevenin's theorem to the MCR circuit, the equivalent schematic shown in Figure 4 is obtained.

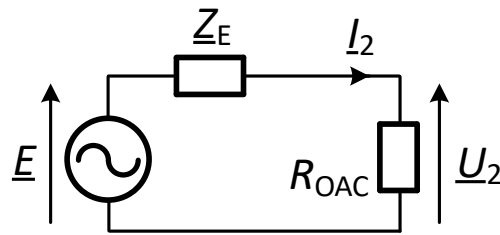


Figure 4. Thevenin's equivalent of MCR circuit.

The equivalent circuit is described by the following equations:

$$E = \frac{U_1 k \sqrt{X_{L1} X_{L2}}}{X_{L1} - X_{C1}}, \quad (5)$$

$$Z_E = j(X_{L2} - X_{C2}) - j \frac{k^2 X_{L1} X_{L2}}{X_{L1} - X_{C1}}. \quad (6)$$

It is obvious that the output voltage U_2 is independent of the load resistance R_{OAC} ($U_2 = E$) when:

$$Z_E = 0. \quad (7)$$

Condition (7) is met, among others, for:

$$\begin{aligned} X_{C1} &= X_{L1}(1 - k^2), \\ X_{C2} &= 0. \end{aligned} \quad (8)$$

The output to input voltage ratio U_O/U_I is equal to the ratio of U_2 to U_1 (1). By using Equations (5), (7), and (8), it is obtained:

$$\frac{U_O}{U_I} = \frac{U_2}{U_1} = \frac{E}{U_1} = \frac{1}{k} \sqrt{\frac{X_{L2}}{X_{L1}}}. \quad (9)$$

Therefore, if the coupling coefficient k is in the order of 0.9 and the coils' self-reactance X_{L1} and X_{L2} are similar, the output voltage will be approximately 10% higher than the input voltage.

Equation (8) will be used for the design process of the MCR circuit. In this case the input impedance of the circuit is:

$$Z_1 = \frac{U_1}{I_1} = \frac{R_{OAC} k^2 X_{L1} X_{L2}}{R_{OAC}^2 + X_{L2}^2} + j \frac{R_{OAC}^2 k^2 X_{L1}}{R_{OAC}^2 + X_{L2}^2} \quad (10)$$

and remains inductive for any resistance value. This is beneficial due to the use of a resonant voltage source inverter (Figure 2). Considering the non-zero parasitic resistances of the coils, the efficiency of the MCR circuit can be estimated using the following equation:

$$\eta = 1 - \frac{\Delta P}{P_{1AC}} = 1 - \frac{R_{p1} I_1^2 + R_{p2} I_2^2}{\text{Re}[\underline{U}_1 \underline{I}_1^*]} = 1 - \frac{R_{p2}}{R_{OAC}} - \frac{R_{p1}}{R_{OAC}} \frac{R_{OAC}^2 + X_{L2}^2}{k^2 X_{L1} X_{L2}} \quad (11)$$

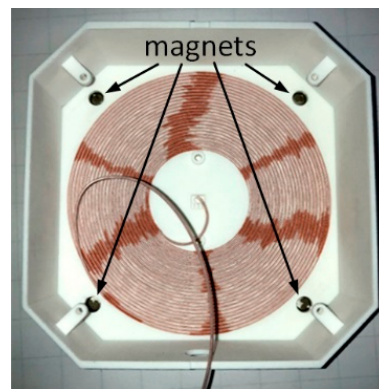
where ΔP is equal to power losses in the coils, P_{1AC} is equal to the input power of the circuit, I_1 and I_2 are RMS values of input and output currents. The output to input voltage ratio is given as:

$$\frac{U_O}{U_I} = \frac{U_2}{U_1} = \frac{\sqrt{[k\sqrt{X_{L1}X_{L2}}(R_{OAC} - R_{p2}) - R_{p1}X_{L2}]^2 + R_{OAC}^2R_{p1}^2}}{R_{OAC}k^2X_{L1}} \quad (12)$$

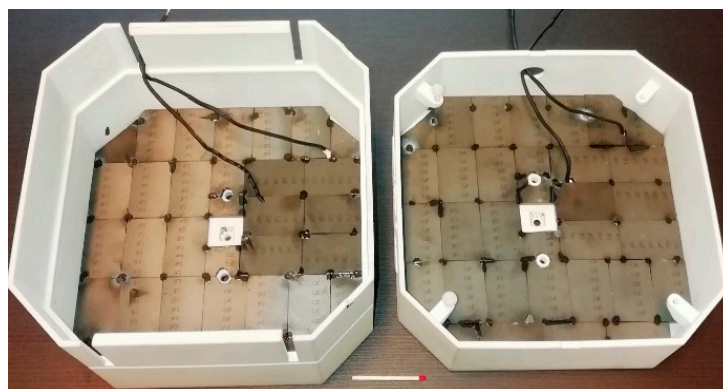
4. Prototype of IPT-IMD System

4.1. MCR Circuit

The MCR circuit has been built based on the analysis results presented in Section 3. The single-layer and spiral coils (outside diameter: 83 mm, inside diameter: 35 mm) were wound with 24 turns of litz wire (Figure 5a). They are well fitted to the plastic casings. 3F3 ferrite plates (PLT38, E series— $25 \times 38 \times 3.8 \text{ mm}^3$) were used to shield and increase both the self- and mutual inductances of the coils. The magnetic shields were placed outside of the coils (Figure 5b). Additionally, aluminum plates were used on the outside to improve the shielding effect and at the same time provide more effective cooling (Figure 5c). The aluminum plates were cut accordingly to avoid additional power losses due to eddy currents.



(a)



(b)

Figure 5. Cont.

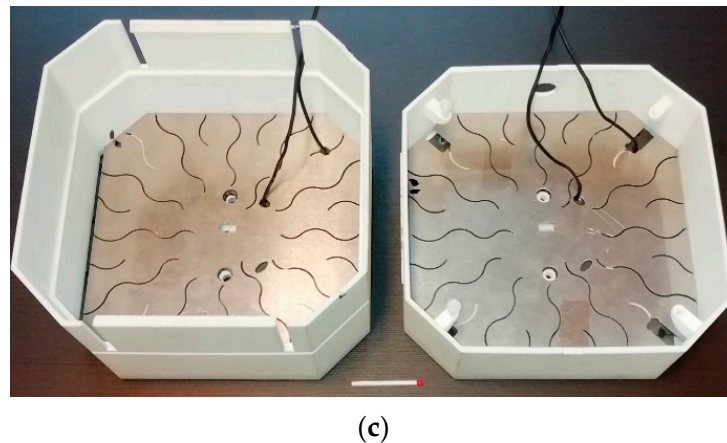


Figure 5. Coils of MCR circuit: (a) primary coil, (b), coils with magnetic shields, (c) coils with magnetic shields and aluminum plates.

The coils, magnetic shields and aluminum plates were placed in the dedicated plastic casings (Figure 5). The casings ensure a stable position of the coils and their coaxial arrangement. The distance of 12 mm between the coils results directly from the applied casings and their mounting position. The parameters of the coils were measured with an Agilent 4294A impedance analyzer at the frequency of 150 kHz. The measurement results are summarized in Table 1.

Table 1. Parameters of magnetically coupled coils.

	$L_1, \mu\text{H}$	Q_1	R_{p1}, Ω	$L_2, \mu\text{H}$	Q_2	R_{p2}, Ω	k
Coils without shielding	76.8	240	0.30	76.5	247	0.29	0.65
Coils with magnetic shields	234	305	0.72	231	313	0.70	0.87
Coils with magnetic shields and aluminum plates	229	218	0.99	227	223	0.96	0.87

Using Equation (8) and assuming the frequency ($f = 150$ kHz), the coupling coefficient ($k = 0.87$) and the primary coil inductance ($L_1 = 229 \mu\text{H}$), the required primary-side compensation capacitance was calculated ($C_1 = 20.2$ nF). Based on Equation (12) and Table 1, assuming the input voltage (e.g., $U_I = 300$ V) and the output power (e.g., $P_O = 1200$ W), the output voltage ($U_O = 330$ V, $U_O/U_I = 1.1$) was iteratively calculated. This operation point corresponds to $R_{ODC} = 90.8 \Omega$ and $R_{OAC} = 73.6 \Omega$ (2), respectively. Finally, according to Equation (11), the efficiency ($\eta = 97\%$) was found.

4.2. Control Method

The control method of the IPT subsystem is explained in Figure 6. Figure 6a shows a simplified diagram of the IPT subsystem control. The control includes a proportional-integral (PI) controller that aligns the DC output voltage U_O with the DC supply voltage U_I . The voltage U_I is measured and, using an additional rate limiter, is entered into the PI controller as a reference signal U_{OREF} . In turn, the feedback signal (U_O) is provided via an optical link. The output of the PI controller is the phase shift angle Φ between control signals of both the inverter half-bridges (pulse width modulation (PWM) control method) as explained in more detail in Figure 6b. The primary-side inverter (T_1, T_2, T_3, T_4) is controlled by a field-programmable gate array (FPGA)-based system. The switching frequency f is set to 150 kHz. The inverter is inductively loaded, thus hard commutations are avoided. The VFD microprocessor system controls the optical link transmitter according to the PWM method. The signal has a fixed frequency of 20 kHz and the duty cycle carries the information about the output voltage U_O . The optical link is placed in the center of the coils, within the primary and secondary casings. The VFD integrated on the secondary-side

with the motor is a standalone unit, controlled by a microprocessor system, ensuring the stabilization of the angular velocity of the motor in a wide range of load variations.

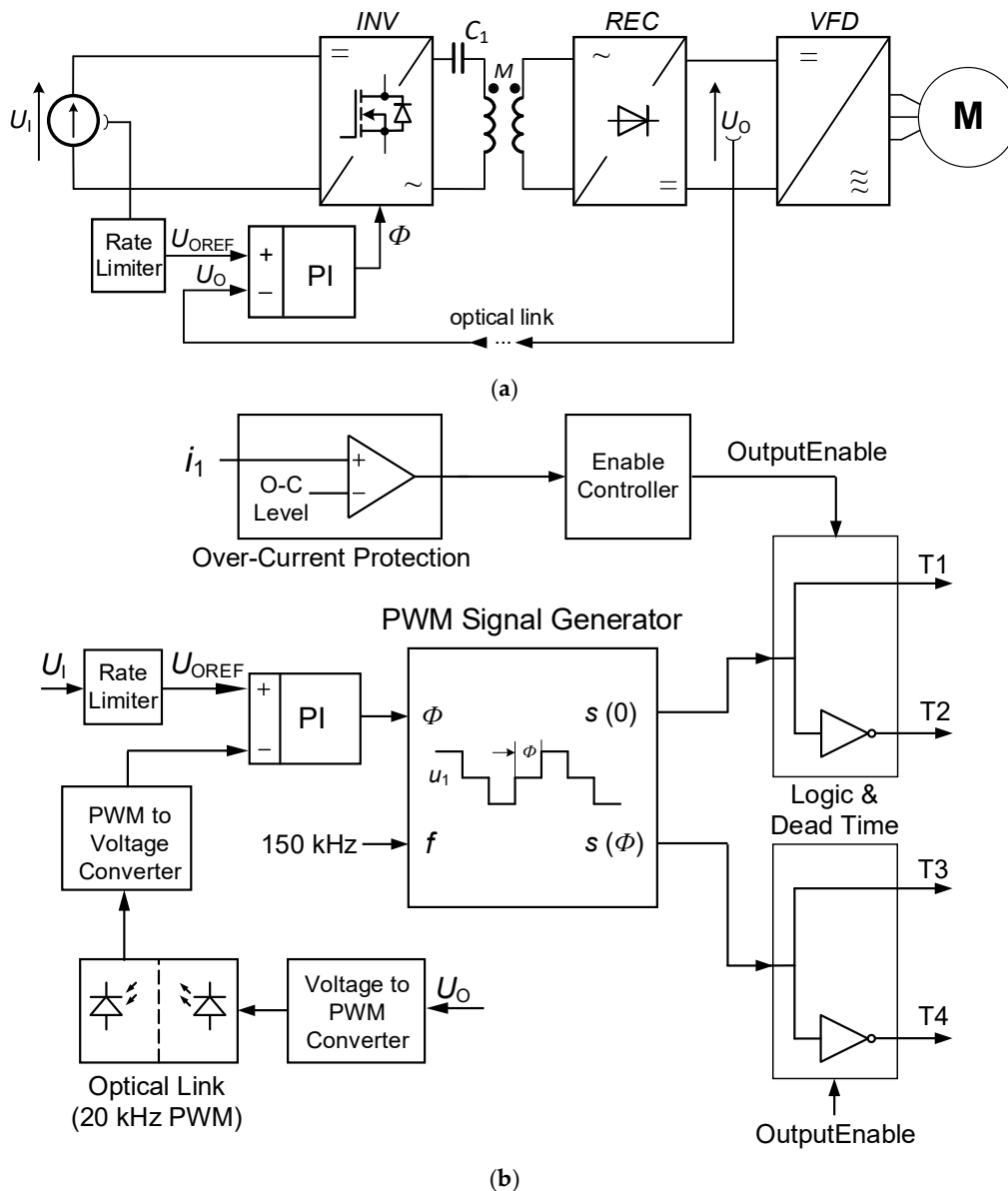


Figure 6. Control block diagrams: (a) simplified, (b) detailed.

A soft-start of the system is required to safely pre-charge the capacitors C_O on the VFD. This is done when the connected IPT-IMD system is started for the first time, or after the primary coil is put in its place (as for a regular plug). The pre-charge process is realized by limiting the rate of the reference signal U_{OREF} at the input of the PI controller. An over-current protection, which turns off the inverter when its load current threshold is exceeded, is also implemented. This can occur, for example, when the motor is overloaded or when the coils are accidentally decoupled. The settings of the PI controller are not critical as the response time is also deliberately limited by the rate limiter during normal operation. It is an order of magnitude faster than for the system soft-start. This solution has been applied due to the relatively large capacitance of the rectifier filter to avoid unnecessary overloading of the IPT system.

4.3. IPT-IMD System

The IPT-IMD system prototype is depicted in photographs in Figure 7. Figure 7a presents its primary-side: the inverter (INV), the resonant capacitor (C_1), the primary casing (PC) with the shielded coil and the receiver-side of the optical link (OL). The inverter uses TP65H035WS cascode GaN FETs as power semiconductors. The inverter control system is based on an Artix-7 FPGA (100 MHz, 32 MB). The optical link is placed outside the casings for measurement purposes. Figure 7b presents the secondary-side of the prototype: the electric motor (M) with the VFD and the capacitors C_O , the secondary casing (SC) with the shielded coil, the rectifier (REC) and the transmitter-side of the optical link (OL). The rectifier printed circuit board (PCB) is placed outside the casing for measurement purposes only. It is actually mounted on the aluminum plate inside the casing. The main system parameters are summarized in Table 2.

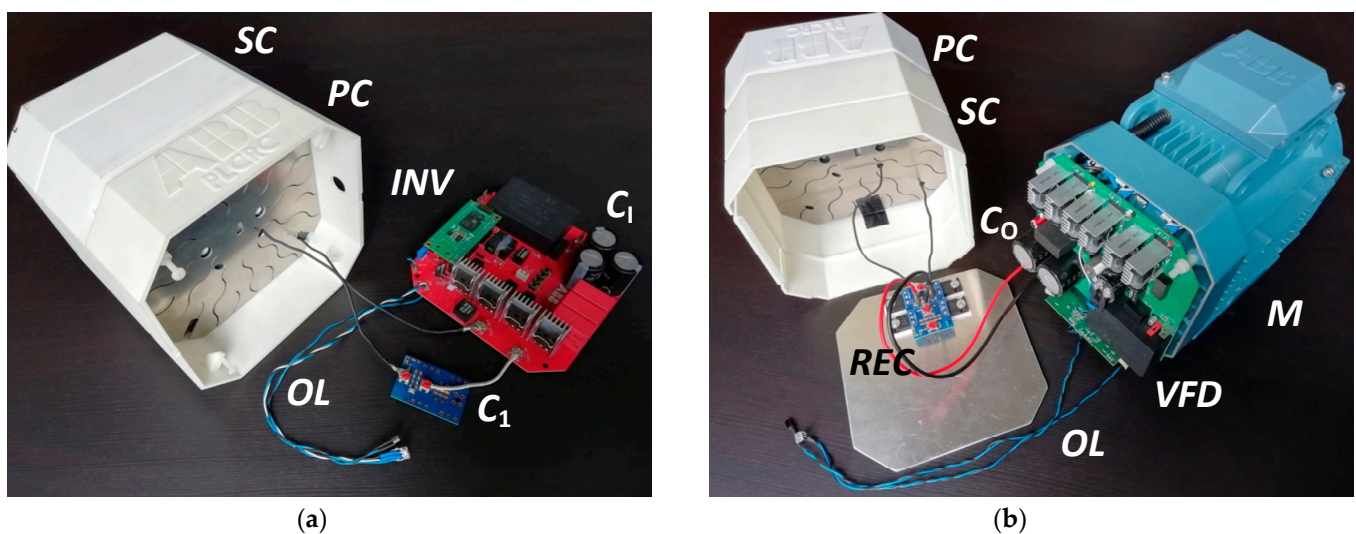


Figure 7. Photographs of IPT-IMD system prototype: (a) primary-side, (b) secondary-side.

Table 2. Parameters of IPT-IMD system.

Parameter	Value	Description
U_I	100–300 V	DC power supply, 300 V/5 A
C_1	810 μ F	$3 \times 270 \mu$ F on INV PCB
T_1 – T_4	650 V/29.5 A	TP65H035WS, GaN FETs
C_1	20.85 nF	MLCC C0G
D_1 – D_4	650 V/10 A	STPSC20H065 SiC Diodes
C_O	940 μ F	$2 \times 470 \mu$ F on VFD PCB
R_{ODC}	35–900 Ω	laboratory resistor
VFD	3-phase inverter, $6 \times$ TP65H035WS, GaN FET-based	
Motor	3-phase, 1.5 kW, 1445 rpm, 230/400 V, M3AA090LD4 (delta configuration with nominal voltage of 230 V)	

5. Experimental Results

The measurements were carried out in a laboratory setup corresponding to the schematic shown in Figure 2. The main aim of the experimental tests focused on the IPT subsystem was to determine its AC/AC and DC/DC efficiencies and the dependence of its output voltage U_O on the output power P_O . As this subsystem can be considered individually for much easier and more comprehensive testing, its DC output was loaded with a laboratory resistor R_{ODC} . This equivalent resistor replaces the IMD subsystem.

Additionally, the VFD was also connected to the DC output, but only its input capacitor bank was used. All measurements were conducted using a Yokogawa WT5000 power analyzer. The following quantities were recorded to illustrate the system performance (Figure 2):

- DC parameters ($P_I = U_I I_I$ —DC input power, $P_O = U_O I_O$ —DC output power, $\eta_{DC} = P_O/P_I$ —DC/DC efficiency),
- AC parameters ($P_{1AC} = \frac{1}{T} \int_0^T u_1 i_1 dt$ —AC input power, $P_{2AC} = \frac{1}{T} \int_0^T u_2 i_2 dt$ —AC output power, $\eta_{AC} = P_{2AC}/P_{1AC}$ —AC/AC efficiency, where $T = \frac{1}{f}$ —switching period).

Figure 8 presents the efficiency measurements as a function of the output power. Both DC/DC and AC/AC efficiencies were recorded at a constant input voltage ($U_I = 300$ and 150 V) in open-loop (η_{DC_O} , η_{AC_O}) and closed-loop (η_{DC_C} , η_{AC_C}) operations. Due to the additional power losses caused by the converters, the DC/DC efficiency is approximately 1 percentage point (p.p.) lower than the AC/AC efficiency. Similarly, the efficiency measured in open-loop operation is approximately 1 p.p. higher than in closed-loop operation. The PWM control of the primary-side inverter is responsible for this efficiency reduction. In simple terms, the conduction time of the transistors is shorter and the inverter zero output voltage interval, where energy is not converted but power losses are generated, is longer. The depicted efficiency curves have a typical shape for IPT systems [28]. The output power changes are caused by load changes, resulting in energy conversion for a different voltage–current relationship. For the input and output voltages of 300 V and the DC output power of 1200 W in closed-loop operation, the distribution of power losses is as follows: 12 W in the inverter (including 4 W for its control), 24 W in the MCR circuit, and 12 W in the rectifier. The AC/AC efficiency was also calculated analytically using Equations (11) and (12) for the output power P_O in the range of 200 to 1200 W at input voltage U_I equal to 300 V. These theoretical results were in the range of 97–98%, corresponding to the measurements.

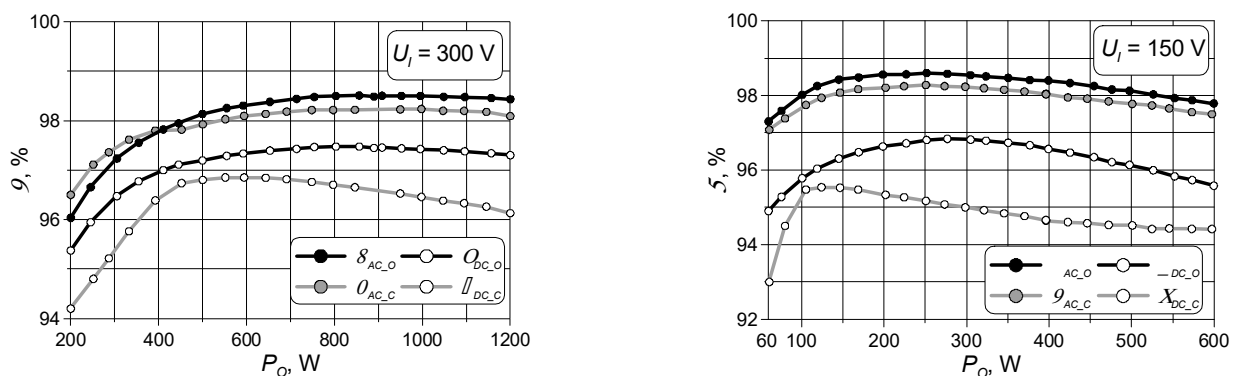


Figure 8. AC/AC and DC/DC efficiencies as a function of output power ($U_I = 300$ and 150 V).

The output voltage measurements under analogous experimental conditions are shown in Figure 9. Both open-loop (U_{O_O}) and closed-loop (U_{O_C}) operations are included. As predicted by the MCR circuit analysis, U_{O_O} is approximately 10% higher than U_{O_C} . The output voltage U_O was also calculated using Equation (12). These theoretical characteristics are within 1% of the measurements (Figure 9).

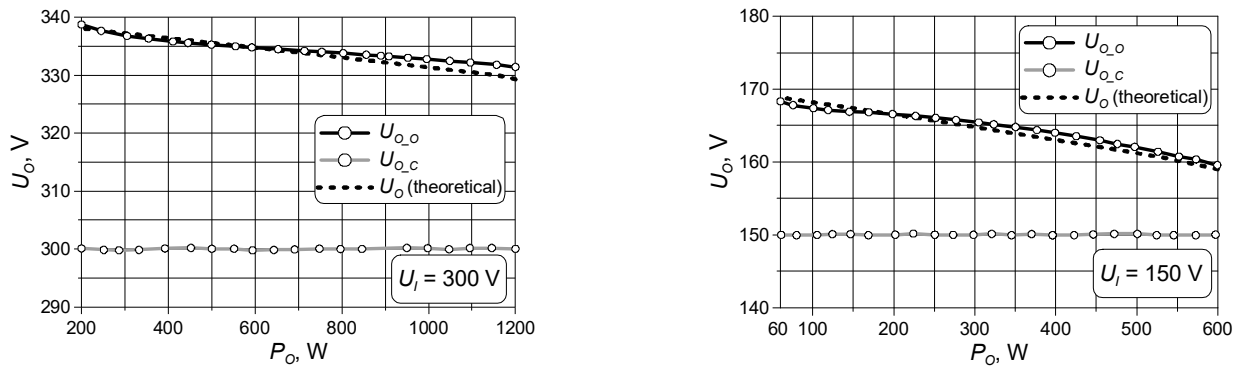


Figure 9. Output voltage as a function of output power ($U_I = 300$ and 150 V).

Figure 10 presents the efficiency measurements as a function of the input voltage, at a constant load resistance ($R_{ODC} = 72 \Omega$) in closed-loop operation. The measurements were recorded for the input voltage U_I in the range of $100\text{--}300$ V. In this case, the AC/AC efficiency is independent of the input voltage. In turn, the DC/DC efficiency varies due to the use of PWM control.

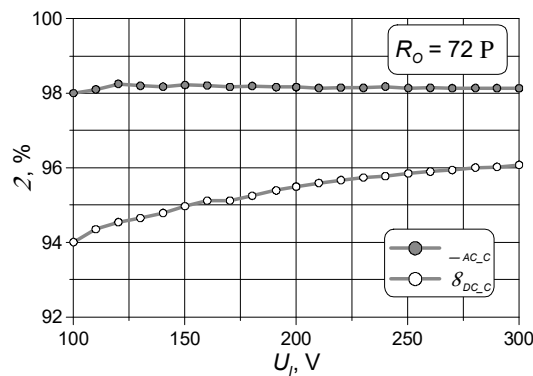


Figure 10. AC/AC and DC/DC efficiencies as a function of input voltage in closed-loop operation ($R_{ODC} = 72 \Omega$).

Figure 11 shows the preliminary experimental results for the whole IPT-IMD system prototype—a graph of the motor angular velocity (no load condition) as a function of the input voltage in closed-loop operation. According to the adopted assumptions, this relationship is linear. Detailed experimental studies of the IMD subsystem and the IPT-IMD system prototype will be presented in a separately prepared paper.

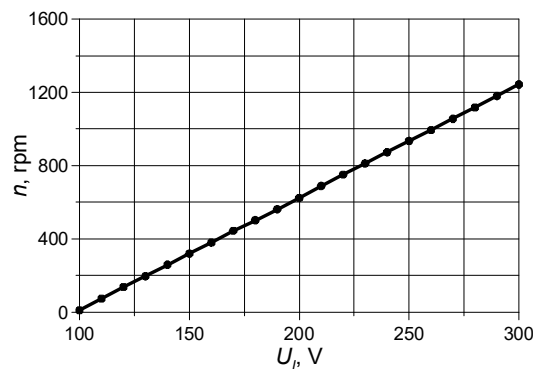


Figure 11. Motor angular velocity (no load condition) as a function of input voltage in closed-loop operation.

Representative voltage and current waveforms of the primary-side inverter and the secondary-side rectifier of the IPT subsystem in the closed loop case are presented in Figure 12. For the tested voltages and powers, the phase shift angle Φ measured with an oscilloscope changed from 37° to 51° , which corresponded to the duty factor D ($D = 1 - \Phi/180^\circ$) in the range of 0.79 to 0.72. These changes are minor due to the applied design method of the MCR circuit—natural load-independent voltage gain.

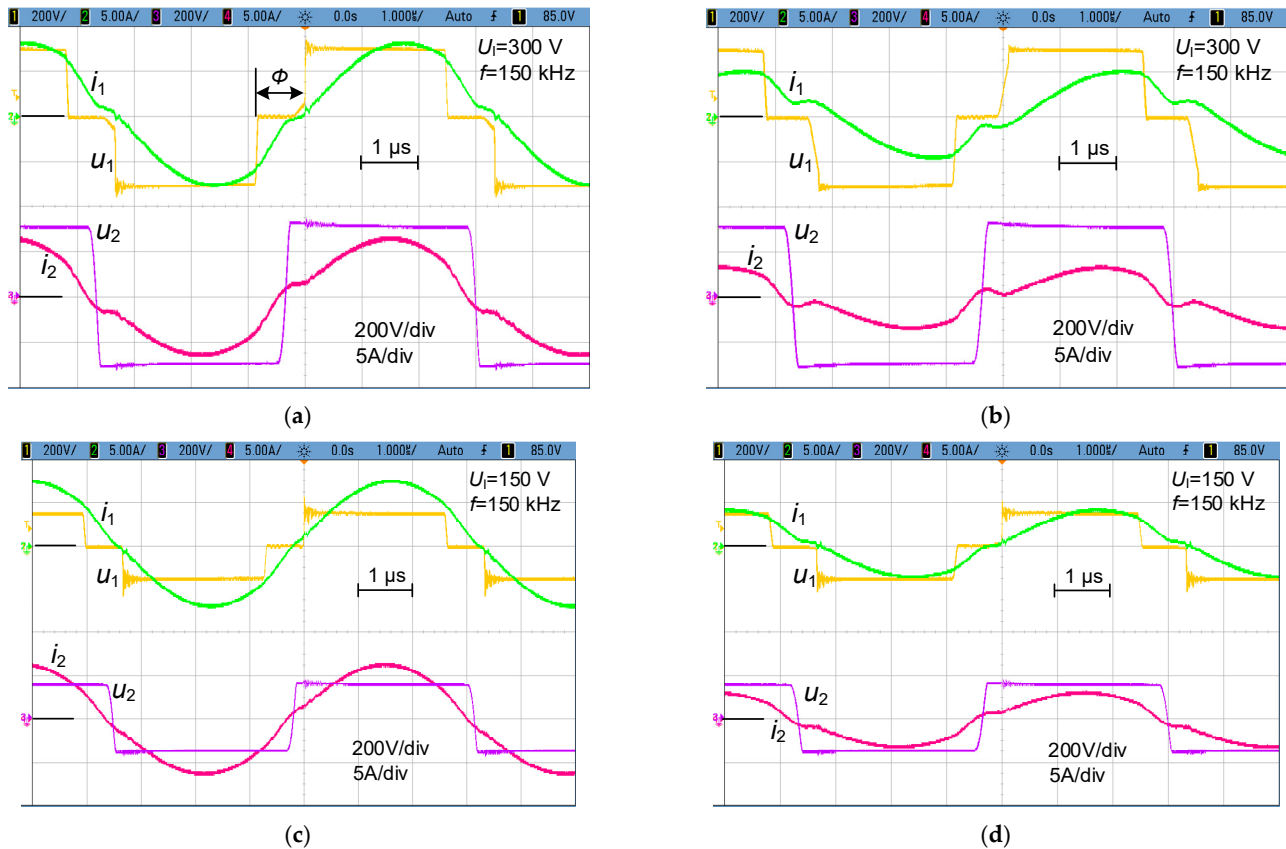


Figure 12. Voltage and current waveforms of primary-side inverter and secondary-side rectifier in closed-loop operation: (a) $U_1 = 300$ V, $P_O = 1200$ W, (b) $U_1 = 300$ V, $P_O = 600$ W, (c) $U_1 = 150$ V, $P_O = 600$ W, (d) $U_1 = 150$ V, $P_O = 300$ W.

Table 3 summarizes the performance of three IPT systems, two representative ones described in [29,31] and the third one presented in this paper. Their geometric parameters are similar. The measured coupling coefficients, coils' self-inductances, switching frequencies, output voltages, and maximum output powers and maximum efficiencies are tabulated. Unfortunately, the efficiencies in [25] are omitted. The IPT subsystem developed in this paper is compact and integrated with motor housing. Its performance are comparable with others, also in closed-loop operation (* in Table 3).

Table 3. Comparison of IPT systems.

	k	$L_1 \sim L_2$, μH	f , kHz	U_O , V	P_{O_max} , kW	η_{AC_max}	η_{DC_max}
[29]	0.71	180	124.5	300–400	1 kW	-	-
[31]	0.8	63	81	90–150	1.4 kW	99%	95%
This paper	0.87	77	150	100–300	1.2 kW	98.6%; 98.2% *	97.5%; 96.9% *

6. Conclusions

The concept of an integrated motor drive has been presented and examined. The developed system is safe, wirelessly powered (“wireless plug”), and allows the angular

velocity of the motor to be changed by setting the input voltage. The system is more complex than a regular motor drive and this complexity results in lower efficiency and can make the system more prone to failure. However, this can be accepted in an industrial environment with an additional benefit. This benefit is the introduction of galvanic isolation, where the IPT transmitter and receiver modules can be freely connected and disconnected by workers not fully qualified to service electrical equipment.

For the given assumptions, the simplified procedure for selecting MCR circuit parameters is explained. A compact prototype of the IPT-IMD system has been built and the IPT subsystem has been experimentally tested. The results confirm feasibility of the system. The AC/AC and DC/DC efficiencies of 96–98.6% and 93–97.5% were recorded for the input voltage of 300 and 150 V, respectively. These conditions corresponded to the output power in the ranges of 200–1200 W (300 V) and 60–600 W (150 V). The efficiencies are approximately 1 p.p. lower in closed-loop operation than in the open-loop case. This is due to the PWM control of the primary-side inverter.

Continuation of studies on the IPT-IMD system will be presented in a separate publication. At the same time, further research should be focused on the system optimization, in particular on its reliability and control methods.

Author Contributions: Conceptualization, A.R., M.K. and Z.K. with contributions from all co-authors; methodology, Z.K. and M.K.; software, K.P., K.K. and K.S.; validation, K.P., K.K., P.Z. and M.K.; formal analysis, Z.K.; investigation, K.P., K.K. and M.K.; resources, A.R., K.S. and Z.K.; writing—original draft preparation, P.Z.; writing—review and editing, P.Z., Z.K., A.R. and K.S.; visualization, M.K., K.P., Z.K., P.Z. and K.S.; supervision, M.K. and A.R.; project administration, M.K. and Z.K.; funding acquisition, M.K. and A.R. All authors have read and agreed to the published version of the manuscript.

Funding: This research was funded by ABB Corporate Technology Center, Cracow, Poland.

Institutional Review Board Statement: Not applicable.

Informed Consent Statement: Not applicable.

Conflicts of Interest: The authors declare no conflict of interest.

References

1. Kaźmierkowski, M.P.; Moradewicz, A.J. Unplugged But Connected: Review of Contactless Energy Transfer Systems. *IEEE Ind. Electron. Mag.* **2012**, *6*, 47–55.
2. Jiang, C.; Chau, K.T.; Liu, C.; Lee, C. An Overview of Resonant Circuits for Wireless Power Transfer. *Energies* **2017**, *10*, 894. [[CrossRef](#)]
3. Zhang, Z.; Pang, H.; Georgiadis, A.; Cecati, C. Wireless Power Transfer—An Overview. *IEEE Trans. Ind. Electron.* **2019**, *66*, 1044–1058. [[CrossRef](#)]
4. RamRakhyani, A.K.; Mirabbasi, S.; Chiao, M. Design and Optimization of Resonance-Based Efficient Wireless Power Delivery Systems for Biomedical Implants. *IEEE Trans. Biomed. Circuits Syst.* **2011**, *5*, 48–63. [[CrossRef](#)]
5. Li, Q.; Liang, Y.C. An Inductive Power Transfer System With a High-Q Resonant Tank for Mobile Device Charging. *IEEE Trans. Power Electron.* **2015**, *30*, 6203–6212. [[CrossRef](#)]
6. Cannon, B.L.; Hoburg, J.F.; Stancil, D.D.; Goldstein, S.C. Magnetic Resonant Coupling As a Potential Means for Wireless Power Transfer to Multiple Small Receivers. *IEEE Trans. Power Electron.* **2009**, *24*, 1819–1825. [[CrossRef](#)]
7. Baszynski, M.; Ruszczuk, A.; Rydygier, P. Wireless energy transfer for industrial applications: Theory, available solutions and perspectives. In Proceedings of the 2016 International Conference on Signals and Electronic Systems (ICSES), Cracow, Poland, 5–7 September 2016.
8. Jawad, A.M.; Nordin, R.; Gharghan, S.K.; Jawad, H.M.; Ismail, M. Opportunities and Challenges for Near-Field Wireless Power Transfer: A Review. *Energies* **2017**, *10*, 1022. [[CrossRef](#)]
9. Houran, M.A.; Yang, X.; Chen, W. Magnetically Coupled Resonance WPT: Review of Compensation Topologies, Resonator Structures with Misalignment, and EMI Diagnostics. *Electronics* **2018**, *7*, 296. [[CrossRef](#)]
10. Wang, C.-S.; Stielau, O.H.; Covic, G.A. Design considerations for a contactless electric vehicle battery charger. *IEEE Trans. Ind. Electron.* **2005**, *52*, 1308–1314. [[CrossRef](#)]
11. Huh, J.; Lee, S.W.; Cho, G.H.; Rim, C.T. Narrow-Width Inductive Power Transfer System for Online Electrical Vehicles. *IEEE Trans. Power Electron.* **2011**, *26*, 3666–3679. [[CrossRef](#)]

12. Han, W.; Chau, K.T.; Zhang, Z. Flexible Induction Heating Using Magnetic Resonant Coupling. *IEEE Trans. Ind. Electron.* **2017**, *64*, 1982–1992. [[CrossRef](#)]
13. Jiang, C.; Chau, K.T.; Leung, Y.Y.; Liu, C.; Lee, C.H.T.; Han, W. Design and Analysis of Wireless Ballastless Fluorescent Lighting. *IEEE Trans. Ind. Electron.* **2019**, *66*, 4065–4074. [[CrossRef](#)]
14. Hao, H.; Covic, G.A.; Boys, J.T. A Parallel Topology for Inductive Power Transfer Power Supplies. *IEEE Trans. Power Electron.* **2014**, *29*, 1140–1151. [[CrossRef](#)]
15. Cheng, C.; Zhou, Z.; Li, W.; Zhu, C.; Deng, Z.; Mi, C.C. A Multi-Load Wireless Power Transfer System With Series-Parallel-Series Compensation. *IEEE Trans. Power Electron.* **2019**, *34*, 7126–7130. [[CrossRef](#)]
16. Dang, Z.; Cao, Y.; Abu Qahouq, J.A. Reconfigurable Magnetic Resonance-Coupled Wireless Power Transfer System. *IEEE Trans. Power Electron.* **2015**, *30*, 6057–6069. [[CrossRef](#)]
17. Chen, L.; Liu, S.; Zhou, Y.C.; Cui, T.J. An Optimizable Circuit Structure for High-Efficiency Wireless Power Transfer. *IEEE Trans. Ind. Electron.* **2013**, *60*, 339–349. [[CrossRef](#)]
18. Ye, Z.; Sun, Y.; Dai, X.; Tang, C.; Wang, Z.; Su, Y. Energy Efficiency Analysis of U-Coil Wireless Power Transfer System. *IEEE Trans. Power Electron.* **2016**, *31*, 4809–4817. [[CrossRef](#)]
19. Liao, Z.; Sun, Y.; Ye, Z.; Tang, C.; Wang, P. Resonant Analysis of Magnetic Coupling Wireless Power Transfer Systems. *IEEE Trans. Power Electron.* **2019**, *34*, 5513–5523. [[CrossRef](#)]
20. Sato, M.; Yamamoto, G.; Gunji, D.; Imura, T.; Fujimoto, H. Development of Wireless In-Wheel Motor Using Magnetic Resonance Coupling. *IEEE Trans. Power Electron.* **2016**, *31*, 5270–5278. [[CrossRef](#)]
21. Jiang, C.; Chau, K.T.; Lee, C.H.T.; Han, W.; Liu, W.; Lam, W.H. A Wireless Servo Motor Drive With Bidirectional Motion Capability. *IEEE Trans. Power Electron.* **2019**, *34*, 12001–12010. [[CrossRef](#)]
22. Jiang, C.; Chau, K.T.; Liu, C.; Han, W. Design and Analysis of Wireless Switched Reluctance Motor Drives. *IEEE Trans. Ind. Electron.* **2019**, *66*, 245–254. [[CrossRef](#)]
23. Zhang, Z.; Chau, K.T.; Qiu, C.; Liu, C. Energy Encryption for Wireless Power Transfer. *IEEE Trans. Power Electron.* **2015**, *30*, 5237–5246. [[CrossRef](#)]
24. Zhang, Y.; Lu, T.; Zhao, Z.; He, F.; Chen, K.; Yuan, L. Selective Wireless Power Transfer to Multiple Loads Using Receivers of Different Resonant Frequencies. *IEEE Trans. Power Electron.* **2015**, *30*, 6001–6005. [[CrossRef](#)]
25. Jahns, T.M.; Dai, H. The past, present, and future of power electronics integration technology in motor drives. *CPSS Trans. Power Electron. Appl.* **2017**, *2*, 197–216. [[CrossRef](#)]
26. Case Note: White Washdown Cut Saw Motor. Available online: https://library.e.abb.com/public/c44fb8d7e1f442d3b64eb8c7374a6376/9AKK106592_0615_Cut%20Saw%20Motors_WEB.pdf (accessed on 25 February 2021).
27. Premium Efficiency Motor Selection and Application Guide. Available online: https://www.energy.gov/sites/prod/files/2014/04/f15/amo_motors_handbook_web.pdf (accessed on 25 February 2021).
28. Motor Handbook. Available online: https://www.infineon.com/dgdl/Infineon-motorcontrol_handbook-AdditionalTechnicalInformation-v01_00-EN.pdf?fileId=5546d4626bb628d7016be6a9aa637e69 (accessed on 25 February 2021).
29. Kuperman, A. Compensation Capacitors Sizing for Achieving Arbitrary Load-Independent Voltage Gain in Series-Series Compensated Inductive WPT Link operating at Fixed Frequency. *IEEE Trans. Power Deliv.* **2020**, *35*, 2737–2739. [[CrossRef](#)]
30. Kaczmarczyk, Z.; Zellner, M. Wireless power transfer with almost constant output voltage at variable load. *Prz. Elektrotech.* **2020**, *96*, 26–31. [[CrossRef](#)]
31. Zhang, Y.; Kan, T.; Yan, Z.; Mao, Y.; Wu, Z.; Mi, C.C. Modeling and Analysis of Series-None Compensation for Wireless Power Transfer Systems with a Strong Coupling. *IEEE Trans. Power Electron.* **2019**, *34*, 1209–1215. [[CrossRef](#)]
32. Zhang, Y.; Yan, Z.; Kan, T.; Liu, Y.; Mi, C.C. Modelling and analysis of the distortion of strongly-coupled wireless power transfer systems with SS and LCC–LCC compensations. *IET Power Electron.* **2019**, *12*, 1321–1328. [[CrossRef](#)]